Journal of *Marine Science and Engineering*

MDPI

Article

Experimental and Numerical Analysis of the Collapse Behaviour of a Cracked Box Girder Under Bidirectional Cyclic Bending Moments

Lei Ao [1,2], Fuyou Li [2,3], Bin Liu [1,2,*], Nan Zhao [4] and Junlin Deng [5,*]

[1] Sanya Science and Education Innovation Park, Wuhan University of Technology, Sanya 572000, China; lei_ao@whut.edu.cn
[2] Green & Smart River-Sea-Going Ship, Cruise and Yacht Research Center, Wuhan University of Technology, Wuhan 430063, China; lifuyou@whut.edu.cn
[3] School of Naval Architecture, Ocean and Energy Power Engineering, Wuhan University of Technology, Wuhan 430063, China
[4] China Ship Scientific Research Centre, Wuxi 214082, China; zhaonan702@126.com
[5] School of Mechanical and Marine Engineering, Beibu Gulf University, Qinzhou 535011, China
* Correspondence: liubin8502@whut.edu.cn (B.L.); junlin.deng@163.com (J.D.)

Abstract

This study presents an integrated experimental and numerical investigation into the collapse characteristics of a cracked box girder subjected to bidirectional cyclic bending moments. An experimental test involving a box girder specimen with a prefabricated transverse crack on the deck panel is conducted under four-point bending to evaluate the influence of cracking on ultimate strength under cyclic loading. The findings are reported through load–displacement curves, strain measurements, and observations of both global and localised structural failure modes, demonstrating strong consistency with finite element simulations conducted using ABAQUS software (version 2022). The results reveal that cyclic loading prior to ultimate capacity induces negligible stiffness reduction in the box girder structure, consistent with the structural behaviour under monotonic loading. The initial failure mechanism is attributed to local buckling of the deck plate, subsequently followed by significant plastic deformation around the crack tips, ultimately leading to global collapse. Parametric studies are carried out to evaluate the influence of key variables on the girder's residual strength, such as crack length, cyclic load amplitude and pattern.

Keywords: ultimate strength; cyclic load; box girder; crack; experiment; finite element analysis

check for updates

Academic Editor: Weicheng Cui

Received: 8 August 2025
Revised: 7 September 2025
Accepted: 14 September 2025
Published: 17 September 2025

Citation: Ao, L.; Li, F.; Liu, B.; Zhao, N.; Deng, J. Experimental and Numerical Analysis of the Collapse Behaviour of a Cracked Box Girder Under Bidirectional Cyclic Bending Moments. *J. Mar. Sci. Eng.* **2025**, *13*, 1802. https://doi.org/10.3390/jmse13091802

Copyright: © 2025 by the authors. Licensee MDPI, Basel, Switzerland. This article is an open access article distributed under the terms and conditions of the Creative Commons Attribution (CC BY) license (https://creativecommons.org/licenses/by/4.0/).

1. Introduction

Ultimate strength evaluation constitutes a fundamental aspect of structural safety assessment in ship design, playing a pivotal role in ensuring structural integrity of in-service ships. Since its incorporation into the IACS (International Association of Classification Societies) Common Structural Rules, assessing the ultimate capacity of hull girders has become a standardised requirement for verifying longitudinal strength over a ship's operational life. Extensive research over recent decades has significantly advanced the understanding of the ultimate strength of ship structures [1–6].

During recent years, the increasing adoption of high-strength steels and larger ship dimensions has resulted in reduced hull girder stiffness, presenting new challenges for ship structural safety. With the advancement in manufacturing high-strength steel that exhibits superior yield strength and toughness, its application in ship structures has enabled the

use of thinner sections and reduced scantlings. While yield strength and toughness govern the initiation of plastic deformation and crack propagation, the dimensions of structural scantlings significantly influence buckling strength. Maintaining a design balance between buckling strength and material yielding necessitates further investigation into the ultimate strength of ship structures.

Structural failure incidents caused by insufficient longitudinal strength still occur (see, for example, Sumi et al. [7]). It indicates that the failure of hull girders in severe sea states is fundamentally a dynamic collapse process involving cyclic loading. Conventional assessment methods, which typically apply a monotonic bending moment under hogging or sagging conditions, fail to adequately capture structural behaviour under cyclic loading conditions. Notably, residual strength following repeated loading can be significantly lower compared to the instantaneous strength observed under the action of monotonic loading, exposing limitations in quasi-static analysis approaches.

Early studies primarily identified plastic accumulation as a failure mechanism, a phenomenon that has recently gained significant attention in ship hull structural analysis under cyclic loading conditions [8–10]. Li et al. [11] examined the ultimate strength of plate structures subjected to cyclic loading combined with lateral load, indicating that the number of cycles has significant effects on the plate's collapse modes. However, their analysis omitted material fracture behaviour, assuming the elastic–perfectly plastic material model. For better predicting residual strain accumulation under cyclic loading, more sophisticated material constitutive laws are required, incorporating a combined isotropic–kinematic hardening model accounting for the Bauschinger effect and cyclic ratcheting, especially for the higher amplitudes and multiple cycles. Chaboche et al. [12] pioneered the development of a mechanical constitutive material model that incorporates mixed hardening behaviour under cyclic loading conditions. Subsequent work by Li et al. [13] and Cui et al. [14] demonstrated that residual strength strongly correlates with the residual plastic strain at the unloading point in cyclic loading; i.e., higher residual strains lead to more pronounced strength reductions. When the applied load remains significantly below the ultimate capacity, the accumulated plastic deformation during cyclic loading is negligible, with each cycle's loading path nearly coinciding with the previous unloading path.

Under the action of longitudinal bending moments, the primary failure mode of a hull girder is typically nonlinear buckling on the compressive side. Recent studies have advanced the understanding of cyclic loading effects [15–17]. Sumi et al. [7] analysed a longitudinal strength failure incident of a container ship, revealing that the bottom plates could buckle at 90% of the ultimate hogging moment. Hu et al. [18] observed rapid box girder strength degradation under bidirectional cyclic loading, while Liu and Guedes Soares [19] demonstrated that cyclic loading can induce local fractures through plastic accumulation. Li et al. [20] introduced an incremental collapse method to evaluate cyclic ultimate structural capacity, finding that material hardening has a negligible impact on global bending response. However, a significant limitation of the existing literature is its predominant focus on numerical simulations, lacking experimental studies to validate these numerical models.

Few experimental investigations have employed simplified box girder specimens due to the complexity of large-scale testing. Deng et al. [21] analysed the ultimate strength of hull girders under unidirectional cyclic loading, in which the applied load reached the structural ultimate strength during the first cycle. The study primarily focused on the post-ultimate strength behaviour of the hull girders, and it did not consider bidirectional cyclic loading that more accurately represents the actual sagging and hogging experienced by ships in service. Song et al. [22] examined the response of a hull girder under bidirectional ultimate loading, pointing out that sustained exposure to ultimate condition leads to a

progressive accumulation of plastic deformation, which reduces structural stiffness. The applied load also reached the ultimate strength within the first cycle, without accounting for the potential influence of cyclic loading below the ultimate strength level.

Nonlinear finite element methods can assist in estimating the structural ultimate capacity of structures, which have been widely applied to simulate various complex behaviours, including geometric and material nonlinearities. Chen et al. [23] utilised nonlinear finite element simulations for the welding process, investigating the influence of heat input variations on the performance of stiffened plates under cyclic loading. Li and Chen [24] analysed the maximum load-carrying capacity of stiffened panels subjected to simultaneous axial cyclic loading and lateral load, revealing a significant decrease in strength under the combined loading conditions. Cui et al. [25] carried out numerical simulations to evaluate how welding-induced deformation and residual stresses affect hull girders' strength under monotonic or cyclic bending moments.

Crack damage is a common and critical issue over the lifetime of ship hull structures in operation, significantly reducing the structural stiffness and load-bearing capacity. While monotonic loading effects on cracked structures have been extensively studied [26–29], recent attention has shifted to cyclic loading scenarios [30–32], revealing complex interactions between crack propagation and plastic accumulation. Cyclic loading can drive crack tip blunting or extension, and excessive load amplitude or a high number of cycles can lead to progressive crack propagation. Xia et al. [33] evaluated the residual strength of five cracked plates subjected to various loading scenarios, observing that the decrease in strength caused by cumulative plastic damage was less pronounced in relatively thicker plates. Hu et al. [34] experimentally analysed the strength degradation behaviour of cracked box girders under ultimate bending moments, and the results indicate that crack propagation accelerates the reduction in ultimate bending moment.

This study explores the residual strength of cracked box girders under cyclic loading, with particular emphasis on pre-ultimate unloading cycle effects. A cracked box girder specimen is designed for cyclic loading tests, with a prefabricated crack on the deck plate. The experimental outcomes, including the load–displacement behaviour, ultimate strength value, and failure modes, are contrasted with the findings from nonlinear finite element simulations. Additionally, the impact of various parameters such as crack length, cyclic load amplitude, and loading pattern on the ultimate loading capacity of cracked hull girders is analysed and discussed.

2. Experimental Details

The experimental programme evaluates the residual strength of a cracked hull girder specimen exposed to cyclic bending moments. A pure bending experiment is conducted for a benchmark study to analyse the ultimate strength behaviour of hull girders subjected to alternating cyclic bending loads.

2.1. Specimen Overview

The specimen's main dimensions are provided in Table 1, while the scantlings of its structural components are presented in Figure 1. The specimen comprises three segments: a central test segment flanked by two support segments on either end. The specimen is reinforced by an orthogonal angle-bar stiffened system at both ends of these segments (L-L for loading and S-S for supporting) to simulate the constraints of transverse bulkheads. A transverse crack (250 mm length $\times$ 10 mm width) is prefabricated on the deck plate of the test segment to simulate an initial imperfection in a ship deck structure. The crack length is set to half the specimen breadth and is located between two longitudinal stiffeners. Since these stiffeners provide crack-arresting capability, the crack is designed to terminate at both

ends against them. This configuration references a mid-span crack scenario in the deck. The crack width was selected to facilitate fabrication.

Table 1. Geometric specifications of the test sample.

Specimen	Unit	Dimension
Overall Length	mm	2400
Test section length	mm	800
Breadth	mm	500
Depth	mm	300
Longitudinal stiffener	mm	FB40 × 5.7
Plate thickness of test segment	mm	2.8
Plate thickness of support segment	mm	4.8
Bulkhead	mm	L75 × 50 × 7.7

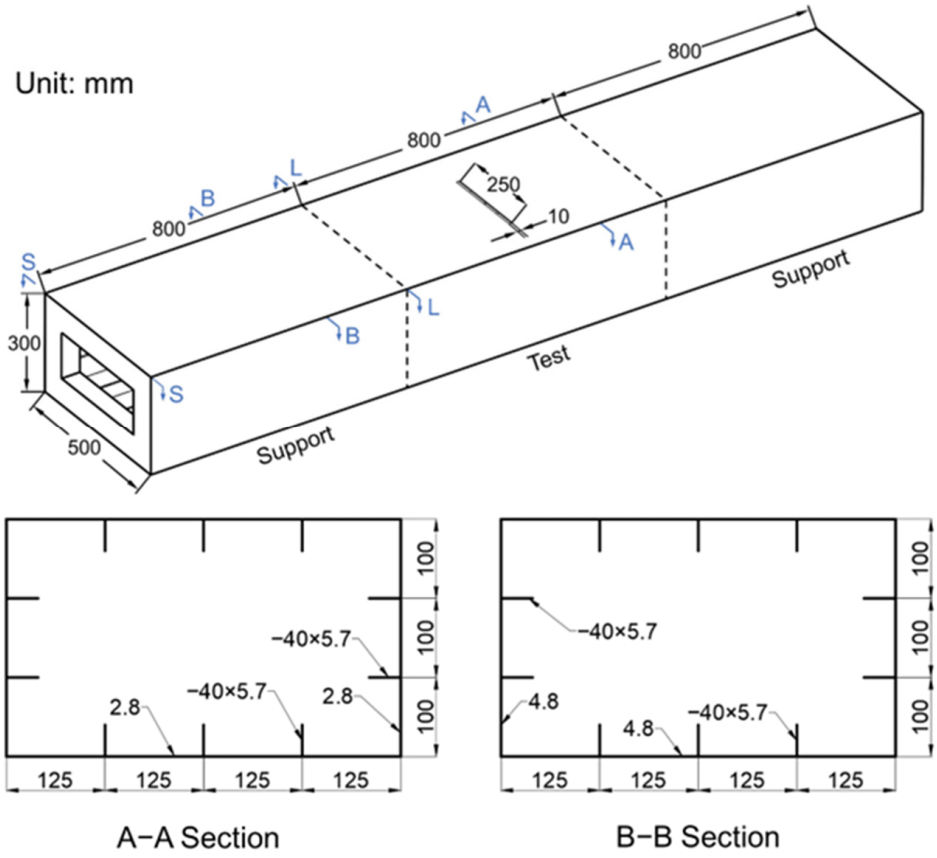


Figure 1. Geometric configuration and main section of the specimen.

The test segment of specimen is fabricated using low-carbon steels with two thicknesses of 2.8 mm and 5.7 mm. Quasi-static uniaxial tensile tests are conducted to characterise the mechanical properties of the steels. [35]. The results of the tensile tests for the two materials are presented in Figure 2, with yield stresses of 299 MPa and 324 MPa, respectively. The resulting engineering stress–strain curves are employed to analyse the material true stress–strain relationship before necking, which is then used for subsequent finite element simulations.

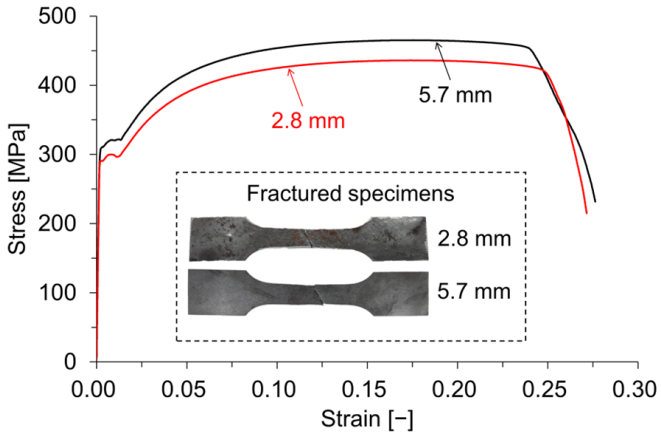


Figure 2. Engineering stress–strain relationship.

2.2. Experimental Setup

A four-point bending configuration is employed to induce vertical bending moments in the specimen, as shown in Figure 3. The specimen is mounted on two round steel bars resting on a rigid foundation (S-S section in Figure 1), in order to simulate the simply supported boundary conditions. Concentrated vertical loads are enforced by a hydraulic cylinder with a bolted loading beam, which transfers the forces to the box girder's cross frames through an additional set of round steel bars (L-L section in Figure 1).

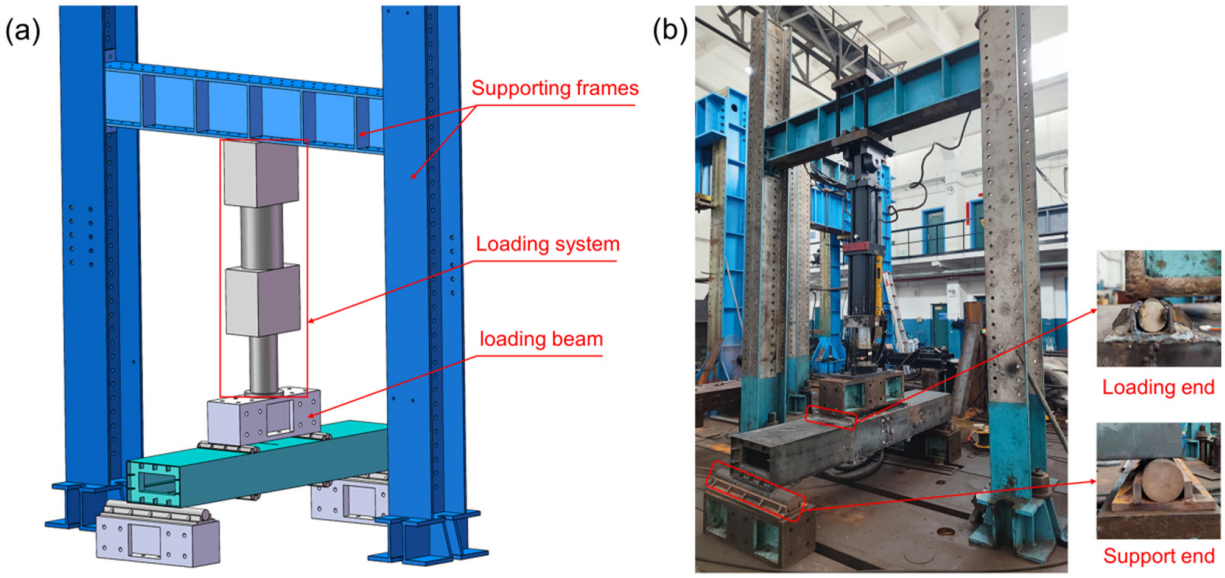


Figure 3. Experimental setup. (**a**) schematic diagram and (**b**) actual image.

The specimen is subjected to bidirectional cyclic loading over five successive loading cycles, with progressively increasing amplitude in each subsequent cycle, and finally is loaded until structural collapse occurs (see Figure 4). In the experiment, the specimen is inverted to achieve forward and reverse loadings, i.e., sagging and hogging bending moments. The initial five loading cycles are force-controlled at a rate of 0.5 kN/s until reaching the given value, while the final loading is applied via displacement control at a rate of 0.05 mm/s until structural collapse. Both force-controlled and displacement-controlled loading are regarded as quasi-static, and the output force is recorded by a load cell in the loading system.

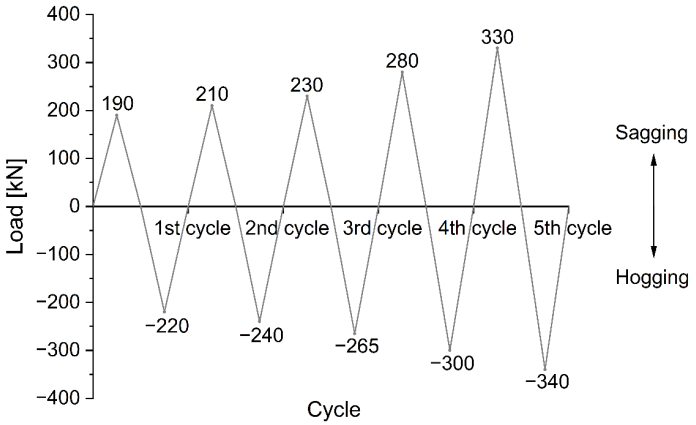


Figure 4. History of cyclic loading in the experiment.

Initial imperfections in the specimen, including initial deformations and welding-induced residual stresses, are inevitably introduced during fabrication. To mitigate their effects, preloading is applied to partially relieve the welding residual stresses, an approach consistent with methods reported in Refs. [5,6]. Consequently, the effect of welding residual stresses is excluded from both the experimental and numerical analyses.

Strain gauges oriented in three directions are installed in areas with expected stress concentrations, especially around the crack tips. Some critical measurement positions are depicted in Figure 5. A preliminary numerical analysis had been undertaken to optimise the gauge arrangement by searching the stress concentration regions.

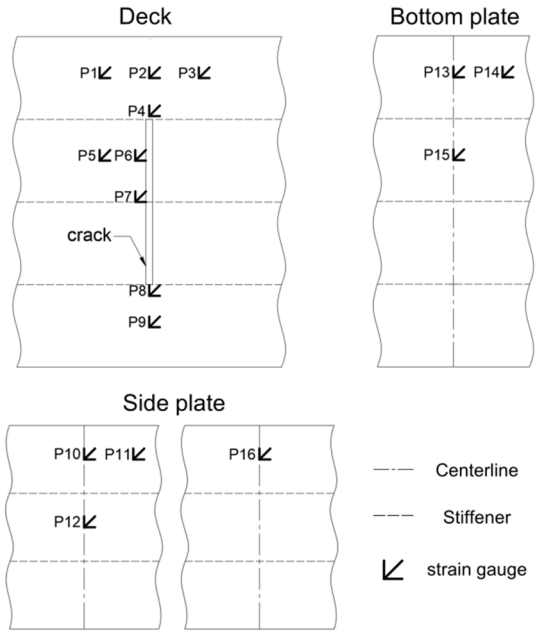


Figure 5. Layout of strain gauges.

Four displacement transducers are positioned at the bottom of the specimen to measure the vertical deflection, as shown in Figure 6. Measurement points D1, D3 and D4 are positioned at the transverse frames of specimen, and D2 is located at the centre of the bottom plate's span. The measured vertical displacements of D1 and D3 can be used to analyse the rotation angle of the test segment by dividing by the length of the support segment (800 mm). The comparison of D1 and D4 can be used to examine the lateral inclination of a specimen.

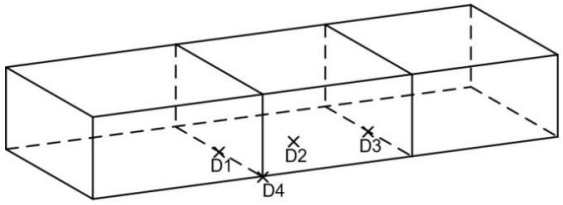


Figure 6. Location of displacement transducers.

The experimental procedure is summarised as follows.

(1) Preparation and preloading phase: Prior to the formal testing, the loading equipment and measurement instruments are calibrated. The specimen is subjected to three preloading cycles within the elastic range to partially release the residual welding stresses and to eliminate any potential interfacial gaps between specimen and test apparatus.
(2) First loading phase: The vertical loading is applied by the hydraulic cylinder in a force-controlled manner and the output force is recorded. After reaching the given load, the load is held for 10 s and then the unloading starts.
(3) Reverse loading and cyclic phase: The specimen is inverted for reverse loading and the displacement transducers are reinstalled. This procedure is repeated through five complete loading cycles.
(4) Ultimate loading phase: In the final monotonic loading stage, the specimen is subjected to displacement-controlled loading until structural collapse occurs. The collapse of a specimen is defined by a sudden large deformation accompanied by a noticeable load decrease. Afterwards, the loading process is immediately terminated, followed by a controlled unloading.

3. Finite Element Model

The nonlinear numerical simulation is conducted analysing the mechanical response of the box test specimen. The numerical model incorporates both geometric and material nonlinearities through an incremental–iterative solution approach based on the Newton–Raphson method. The specimen is modelled using S4R shell elements, which are four-node elements with reduced integration.

The applied loads and boundary constraints in the finite element model are presented in Figure 7. To simulate the simply supported boundary of the support ends, the nodal constraints are applied with Ux = Uy = Uz = 0 and Uy = Uz = 0, respectively. For each loading end, a reference point (RP1 or RP2) is defined at the centre of the loading line coupling with all points along the line. The five cyclic loading stages are implemented under force-controlled conditions to precisely simulate the experimental loading phases, and then the displacement-controlled loading is applied until the collapse of the structure.

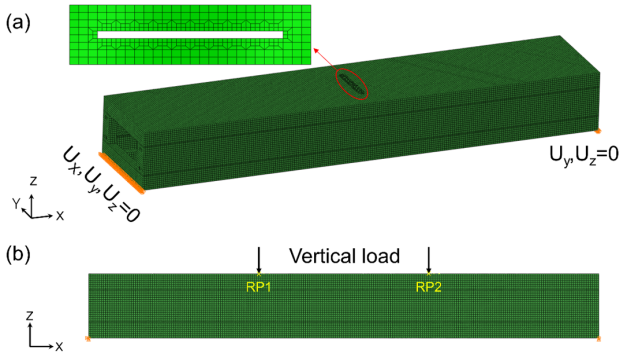


Figure 7. Finite element model of the box girder specimen. (**a**) three-view drawing and (**b**) side view.

The steel material properties are described through an elastic–plastic model that captures the actual stress–strain behaviour. Also, definitions are provided for Young's modulus, Poisson's ratio, and yield strength. The true stress (σ_t) and strain (ε_t) are derived from the engineering stress (σ_e) and strain (ε_e) using the following conversions:

$$\sigma_t = \sigma_e(1 + \varepsilon_e) \tag{1}$$

$$\varepsilon_t = \ln(1 + \varepsilon_e) \tag{2}$$

Initial geometrical imperfections in the specimen's plates and stiffeners are measured, and their overall deformations vary between −3.3 mm and 2.8 mm, as well as −6.9 mm and 7.3 mm, respectively. In the finite element model, imperfections are implemented using empirical formulae (Equations (3) and (4)), with amplitudes set to the measured mean values of 3.1 mm (A_0) and 7.1 mm (B_0) for plates and stiffeners, respectively.

$$w_{0P} = A_0 \sin\frac{m\pi x}{a} \sin\frac{\pi y}{b} \tag{3}$$

$$w_{0S} = B_0 \frac{z}{h_s} \sin\frac{\pi x}{a} \tag{4}$$

where a and b denote the length and width of the plate, respectively; m is the longitudinal mode number of the plate; h_s is the stiffener width.

The mesh convergence analysis results of the finite element model are presented in Figure 8. Three mesh sizes (5 mm, 10 mm and 20 mm) are evaluated, with the refined mesh near the crack region illustrated in Figure 7. The discrepancy in maximum bending load between the 5 mm and 10 mm meshes is only 0.84%, while that between the 10 mm and 20 mm meshes reaches 2.25%. Considering both computational efficiency and accuracy, the mesh size of 10 mm for the overall model and the refined mesh of 5 mm for the crack region are selected in subsequent finite element analyses. The mesh model contains a total of 49,484 elements as well as 49,435 nodes.

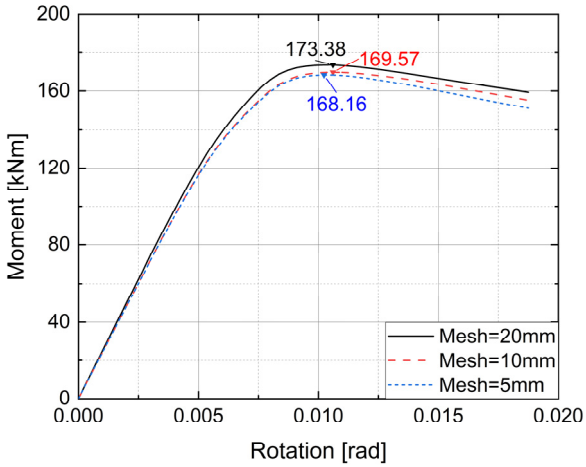


Figure 8. Comparison of bending moment–rotation curves with different mesh sizes.

In summary, the finite element model is developed with careful consideration of mesh selection, inclusion of geometric initial imperfections and the definition of the material constitutive model. These considerations ensure that the numerical simulation accurately captures the mechanical behaviour of cracked structures. The following section presents a comparison between the numerical and experimental results to demonstrate the accuracy of the finite element method.

4. Experiment and Numerical Results

4.1. Bending Moment vs. Rotation Curve

4.1.1. Experimental Result

The bending moment–rotation curves obtained from both experimental testing and numerical simulation for the box girder specimen are presented in Figure 9. The bending moment is obtained by multiplying the applied load at each loading line (half of the total load measured by the load cell) by the moment arm (800 mm). The resulting rotation angle is calculated by the vertical displacements of D1 and D3, presented in Figure 6, dividing by the length of the support segment (800 mm).

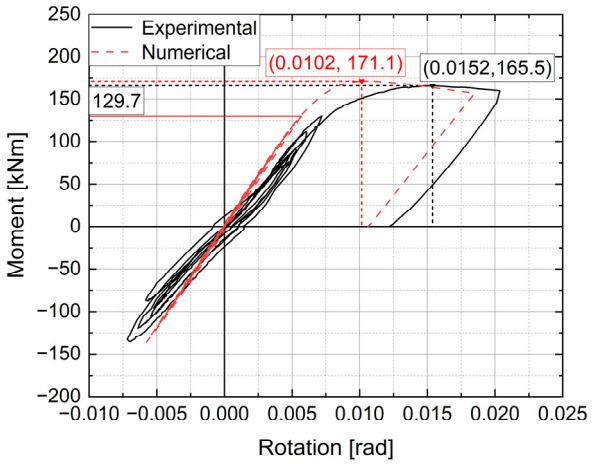


Figure 9. Experimental and simulated bending moment-rotation relationships.

The experimental bending load–rotation curve shows that its slope during the initial five loading cycles closely matches the linear phase of the final monotonic loading, indicating the negligible stiffness degradation due to cyclic loading. During the final monotonic loading phase, the load–displacement relationship remains linear up to a bending moment of 129.7 kNm, beyond which nonlinear behaviour emerges. When the load reaches 165.5 kNm, the specimen attains its ultimate bending capacity, signifying the onset of structural instability. Subsequent loading leads to a gradual decline in moment resistance.

4.1.2. Numerical Result

The numerical ultimate load (171.1 kNm) agrees well with the experimental result (165.5 kNm), showing an error of 3.4%. This slight overestimation in the simulation may be attributed to welding residual stresses remaining in the test model after the preloading stage, which affects the ultimate bending moment. The numerical rotation angle corresponding to the ultimate load is notably smaller than the experimental one (0.0102 rad vs. 0.0152 rad).

Additionally, the elastic stiffness of the numerical curve diverges from the experimental data (see Figure 9). This discrepancy may be due to the experimental setup, where gaps between the round steel bars and the fixed supports cannot be completely eliminated through preloading. Similar phenomena have also been observed in published ultimate pure bending experiments of simple hull girders, as recorded by Xu et al. [36] and Hu et al. [34].

4.2. Collapse Mode

4.2.1. Experimental Result

The experimental final deformation shape of the test segment under the sagging ultimate load is shown in Figure 10. During the initial five loading cycles, no significant deformation is detected near the deck crack or the side shell plate. Although stress concen-

tration and plastic strain accumulation occur near the crack tip under cyclic loading, the resulting plastic strain remains relatively small and insufficient to induce crack propagation. This observation correlates with the bending moment–rotation curve, where structural plastic buckling typically manifests in the nonlinear stage.

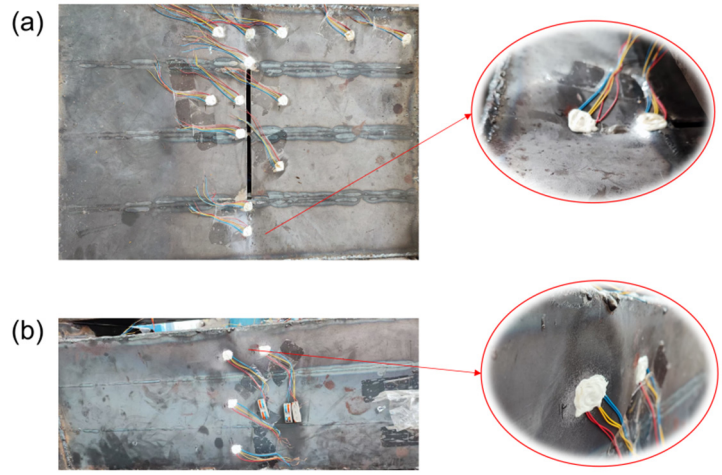


Figure 10. Experimental permanent deformation of (**a**) deck and (**b**) side plates.

As the prefabricated crack reduces the effective cross-sectional area and bending stiffness, the buckling initiates at both crack tips on the deck. Afterwards, the buckling deformation propagates laterally into the adjacent side shell regions, culminating in the global buckling of the specimen. Finally, severe buckling deformation is observed in the region near the crack located on the deck plates as well as the upper side ones.

4.2.2. Numerical Result

The overall and local deformations of the test model obtained from the numerical analysis are displayed in Figure 11. Due to the crack's influence on the stress distribution across the deck, the structural failure of the model is initiated by localised buckling occurring at the crack tips. No significant deformation is observed on either side of the crack. This result aligns well with the experimental findings, confirming the accuracy and reliability of the numerical simulation.

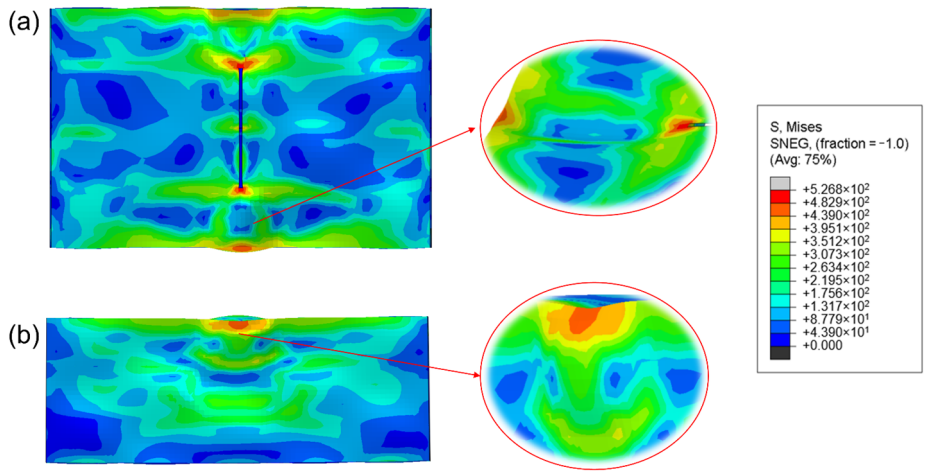


Figure 11. Numerical permanent deformation of (**a**) deck and (**b**) side plates.

Under the ultimate loading condition, the maximum plastic strain obtained at the crack tip element is 0.124. This level of plastic strain, 5 mm in size and 2.8 mm in thickness, is insufficient to initiate crack formation [37]. Furthermore, since no crack propagation was

observed at the crack tip during the experiment, element removal was not incorporated in the finite element analysis.

4.3. Stress

4.3.1. Experimental Result

The experimentally obtained equivalent stresses are derived from the data collected using triaxial strain gauges. The analysed stress values adopt the corresponding material yield stress (299 MPa and 324 MPa) when they exceed this threshold, since the stress calculation formulae in material mechanics are derived based on linear elastic assumptions. The stress values at the stress measurement points under sagging loads are defined as positive, with the corresponding hogging being negative, similar to the cyclic bending moment–rotation curve.

Six representative measurement points on the specimen are selected, and their stresses vs. bending moment curves are plotted in Figure 12. Points P6, P7, P8 and P9 are located around the deck crack, while P10 and P15 are positioned on the side and bottom plate, respectively (see Figure 5). In the first cycle loading stage (C1 in Figure 12), the concentrated stress at the crack front (P8) exceeds the material's yield stress (299 MPa) when the hogging bending moment reaches −88 kNm. In the stress release regions on the free edge of the crack, the stresses in P6 and P7 are much smaller than the one in P8 (Figure 12a,b). Due to the presence of a stiffener at the location of P7, part of the load is transferred to the deck, leading to the yielding of crack tips.

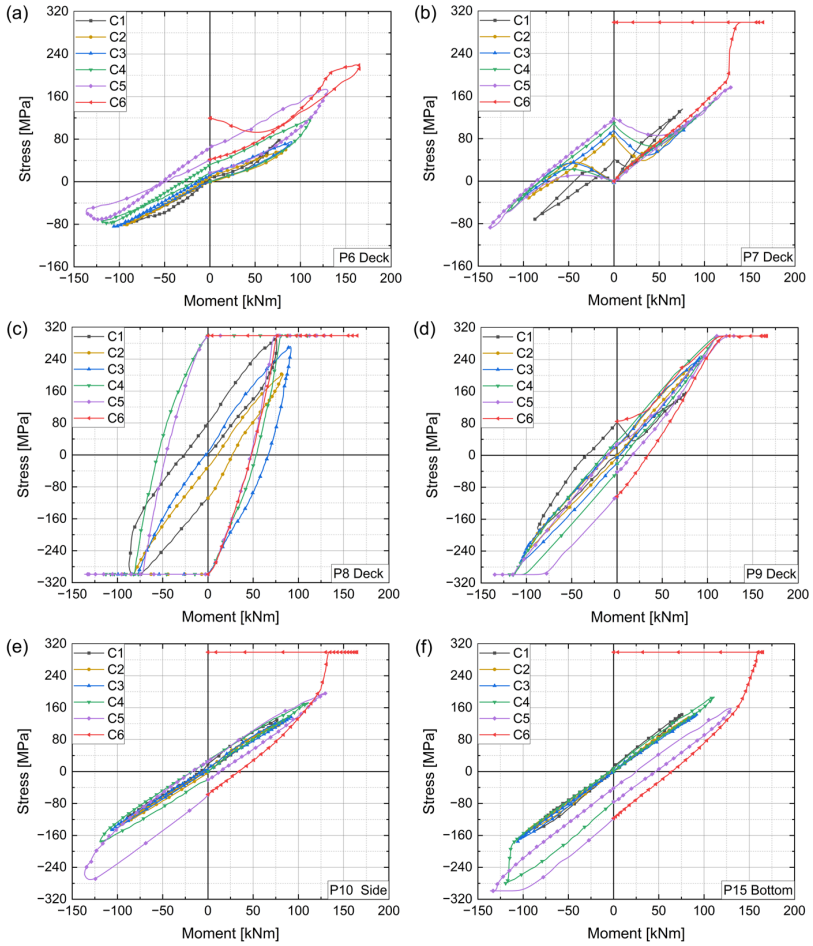


Figure 12. Experimental von Mises stresses at key measurement points on the specimen. (**a**) P6; (**b**) P7; (**c**) P8; (**d**) P9; (**e**) P10; (**f**) P15.

Residual stresses are accumulated at P9 and P15 due to the elastic instability occurring prior to the yield point during the cyclic loading process. This phenomenon is particularly obvious at P15 during the fourth hogging loading cycle (Figure 12f).

In the experiments, some measurement points are positioned symmetrically; for example, points P1 and P3 are longitudinally symmetrical, and points P10 and P16 are transversely symmetrical (see Figure 5). Their stress vs. bending moment curves are plotted in Figure 13, taking the fourth cyclic load as the typical example. Generally, points P1 and P3 exhibit nearly identical cyclic stress paths, indicating the highly symmetrical longitudinal deformation. Points P10 and P16 show some discrepancy during the loading, indicating the different deformations in the transverse direction. This may be attributed to the fact that the initial imperfections affect the structural buckling behaviour.

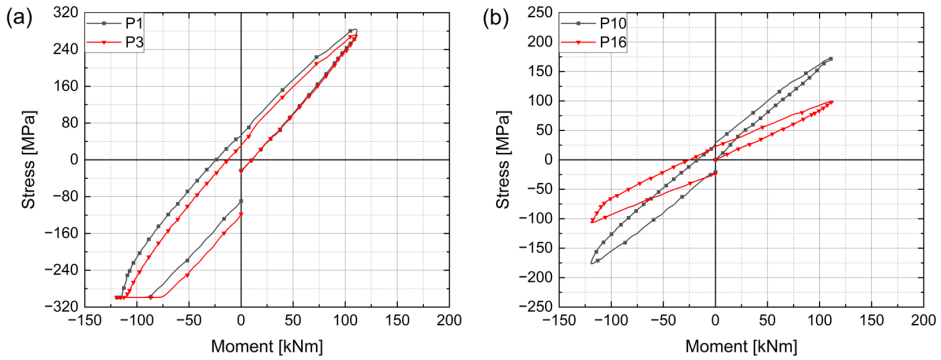


Figure 13. Experimental von Mises stresses of (**a**) P1 vs. P3 and (**b**) P10 vs. P16 during the 4th cycle.

4.3.2. Numerical Result

Figure 14 presents the numerical and experimental stress vs. bending moment curves at two representative measurement points of the structure (P9 on deck plate and P10 on side plate) during the fourth cyclic load. The overall trends of curves are effectively predicted by the numerical simulation. It is observed that the stresses obtained from numerical simulation are slightly lower than the experimental results. This discrepancy may be attributed to the fact that the welding residual stresses are not considered and the initial geometric imperfections of the specimen cannot be perfectly described by the finite element model. Numerous uncertainties inherent in actual structures necessitate certain simplifications in finite element simulations, which inevitably introduce minor discrepancies in the comparison. The stresses exhibit an approximately linear relationship with the applied bending moment during the loading phase, and the residual stresses emerge after unloading as a result of structural buckling.

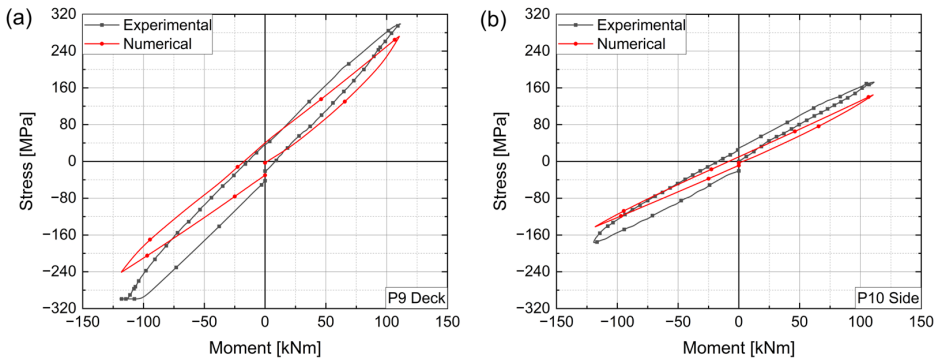


Figure 14. Comparison of experimental and numerical von Mises stresses of (**a**) P9 and (**b**) P10 during the 4th cycle.

5. Discussion

The following subsections explore various factors influencing the cracked hull girders' residual strength, including (1) crack, (2) cyclic load amplitude and pattern, and (3) material model selection.

5.1. Effect of Crack

Numerical comparisons of the bending moment–rotation curves under monotonic and multi-cyclic loadings are given in Figure 15. Generally, the curve in multiple cycles closely follows the path of the curve under monotonic loading, which may be due to the fact that residual plastic strains in multiple cycles slightly affect the structural ultimate strength. Since the applied load level stays beneath the girder's ultimate loading capacity in limited cycle numbers, the accumulated plastic deformation during cyclic loading is negligible, with each cycle's loading path nearly coinciding with the previous unloading path.

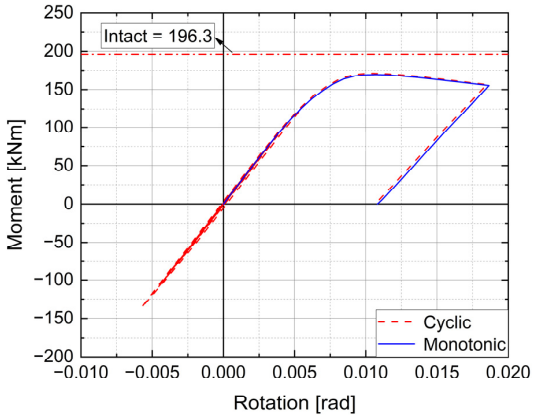


Figure 15. Numerical comparison of the bending load–rotation relationships subjected to monotonic and multi-cyclic loading.

To investigate the crack's effect on the girder's collapse behaviour, one more simulation is performed without crack damage, and the comparative results are shown in Figure 15. The intact model exhibits a maximum flexural moment of 196.3 kNm, while the presence of the crack leads to a notable reduction (12.8%) in sagging conditions.

To systematically investigate the crack length effects, the dimensionless crack length ratio is introduced, where c represents crack length and b denotes specimen width (500 mm). Here, three specific ratios (c/b = 0.25, 0.5 and 0.75) are selected, and the resulting bending moment–rotation curves are shown in Figure 16. It reveals that the reduced initial stiffness of cracked specimens strongly affects the structural ultimate strength.

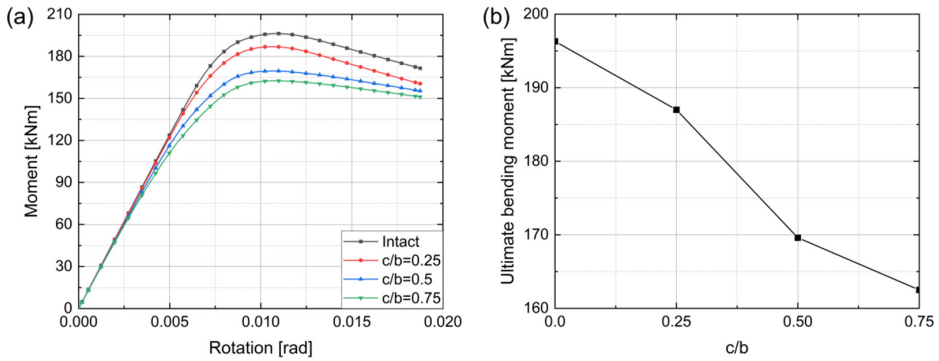


Figure 16. Influence of crack length under monotonic bending. (**a**) Bending moment vs. rotation curves and (**b**) Ultimate bending moment vs. crack length curve.

The ultimate strength exhibits a nearly linear reduction as the length of the crack grows, with a maximum decrease of 17.2% observed at c/b = 0.75. Notably, the rotation angle at ultimate loading remains relatively constant across all crack lengths. This indicates that crack growth primarily affects structural strength, while its effect on deformation is minimal.

5.2. Effect of Cyclic Load

5.2.1. Load Amplitude

In the previous numerical simulations, the maximum cyclic bending load and the final ultimate flexural moment are 136.0 kNm and 171.1 kNm, respectively. To analyse the effect of cyclic load amplitude, two larger cyclic bending moments (148 kNm and 164 kNm) are selected. In the loading process, five bidirectional cyclic loadings and a final monotonic ultimate loading are carried out.

As illustrated in Figure 17, the residual angular displacement at zero load increases with the magnitude of cyclic loading due to the accumulation of inelastic deformation. It also means that the unloading path deviates slightly from the initial loading path in the case of a cyclic bending moment of 164 kNm. However, these phenomena slightly affect the girder's residual strength, as the failure mode is primarily governed by buckling behaviour without crack propagation.

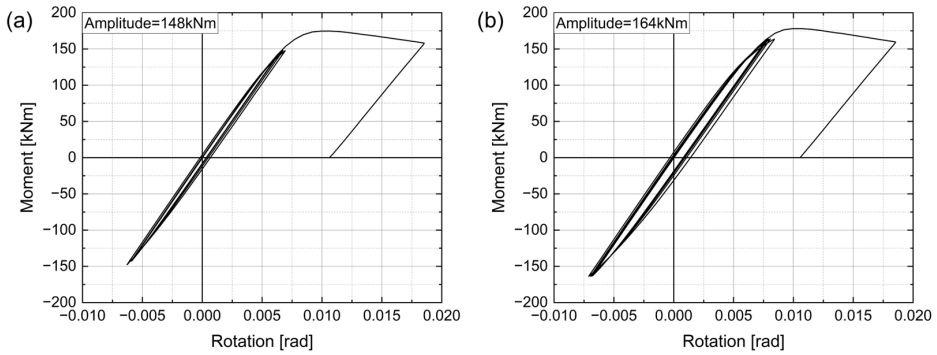


Figure 17. Bending moment–rotation curves under cyclic loading with amplitudes of (**a**) 148 kNm and (**b**) 164 kNm.

5.2.2. Unidirectional Cyclic Loading

The effect of unidirectional cyclic loading on the hull structure's loading capacity was examined experimentally and numerically by Paik et al. [38], Deng et al. [21] and Song et al. [39]. Here, a numerical investigation into the ultimate strength of the test model subjected to unidirectional cyclic loading is carried out, compared to the effect of bidirectional cyclic loading (Figure 18). It is observed that the loading and unloading curves exhibit nearly identical paths, since the applied cyclic loading does not cause significant buckling deformation of the specimen.

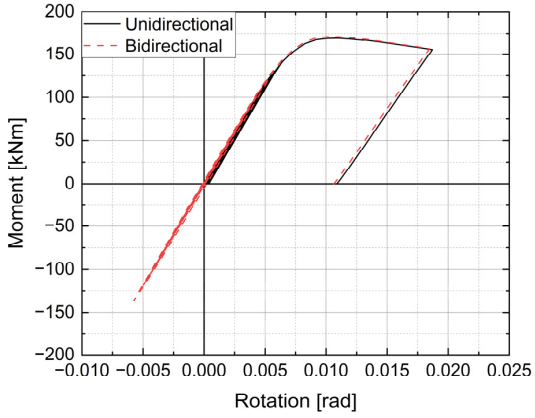


Figure 18. Bending moment–rotation curves under unidirectional and bidirectional cyclic loadings.

5.3. Effect of Material Model

The elastic–perfectly plastic material model is commonly used in the evaluation of thin plate structures' failure strength. To analyse the effect of simplification of the material model, one more simulation is performed in comparison with the definition of the true stress–strain relationship of the material. In the simplified elastic–plastic material model, the stress keeps constant after reaching the material yield point (299 MPa and 324 MPa). Their comparison using the flexural load–rotation curves is presented in Figure 19.

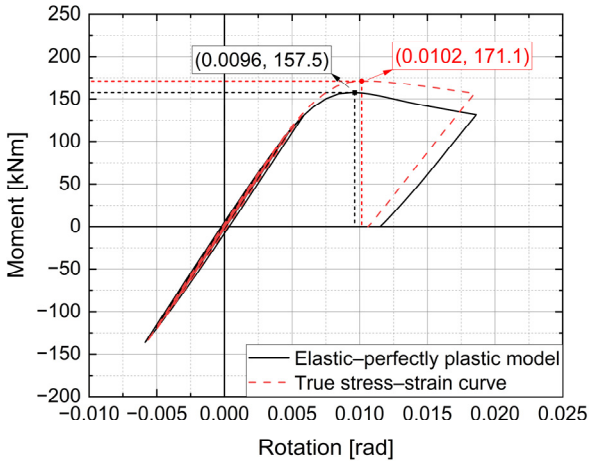


Figure 19. Comparison of material model selection using elastic–perfectly plastic model and true stress–strain curve.

Compared to the implementation of a true stress–strain curve, the use of the elastic–perfectly plastic model means that the nonlinear stage is reached earlier with a smaller rotation angle at ultimate loading. The resulting ultimate bending capacity for the elastic–perfectly plastic model is 157.5 kNm, with a 7.9% reduction compared to the case of the true stress–strain curve (171.1 kNm). This discrepancy is mainly due to the elastic–perfectly plastic model ignoring post-yield hardening behaviour of the material, which ultimately results in an underestimation of the structural ultimate strength.

6. Conclusions

The present research has addressed combined experimental and numerical investigations into the ultimate strength of a cracked box girder under bidirectional cyclic bending moments, illustrating the gradual collapse behaviour of the damaged structure.

The reduction in the ultimate strength of a structure due to cracking can be attributed to two primary factors: crack propagation at the tip leading to structural fracture failure and reductions in bending stiffness causing premature buckling failure. In the present experiment, the collapse of the hull girder was primarily governed by buckling phenomena without crack propagation. Local buckling occurs firstly at both ends of the crack and then gradually propagates to side plates, leading to global structural collapse. For real ship structures, the dominant failure mechanism, whether fracture or buckling, depends on the specific structural characteristics and requires further investigation.

At load levels significantly below the maximum load-carrying capacity of the structure, the accumulated plastic deformation during cyclic loading is negligible. The variation in the load amplitude and loading mode has no noticeable influence on the girder's ultimate strength within a constrained number of cycles. The application of the elastic–perfectly plastic material model causes a significant reduction in the structural ultimate strength based on numerical analysis.

In the present experiment, both the amplitude and number of cyclic loadings were limited. Future research could apply the loads closer to the structural ultimate strength under an increased number of cycles. Furthermore, since the welding residual stresses were not accurately quantified, their uncertainty introduced limitations in the result analysis. Future research could incorporate advanced measurement techniques to obtain precise data on these stresses.

Author Contributions: Conceptualization, L.A., F.L. and B.L.; methodology, L.A. and F.L.; software, F.L.; validation, L.A.; writing—original draft preparation, L.A. and F.L.; writing—review and editing, B.L., N.Z. and J.D.; supervision, L.A. and B.L. All authors have read and agreed to the published version of the manuscript.

Funding: This research was funded by the National Natural Science Foundation of China (Grant No. 52271326; 52301385; 52161042) and the Natural Science Foundation of Guangxi Province (Grant No. 2025GXNSFAA069191).

Institutional Review Board Statement: Not applicable.

Informed Consent Statement: Not applicable.

Data Availability Statement: Data presented in this article are available upon request from the corresponding author.

Conflicts of Interest: The authors declare no conflicts of interest.

References

1. Saad-Eldeen, S.; Garbatov, Y.; Guedes Soares, C. Effect of corrosion severity on the ultimate strength of a steel box girder. *Eng. Struct.* **2013**, *49*, 560–571. [CrossRef]
2. Garbatov, Y.; Saad-Eldeen, S.; Guedes Soares, C. Hull girder ultimate strength assessment based on experimental results and the dimensional theory. *Eng. Struct.* **2015**, *100*, 742–750. [CrossRef]
3. Kim, D.K.; Lim, H.L.; Yu, S.Y. A technical review on ultimate strength prediction of stiffened panels in axial compression. *Ocean Eng.* **2018**, *170*, 392–406. [CrossRef]
4. Li, S.; Kim, D.K.; Benson, S. The influence of residual stress on the ultimate strength of longitudinally compressed stiffened panels. *Ocean Eng.* **2021**, *231*, 108839. [CrossRef]
5. Liu, B.; Gao, L.; Ao, L.; Wu, W. Experimental and numerical analysis of ultimate compressive strength of stiffened panel with openings. *Ocean Eng.* **2021**, *220*, 108453. [CrossRef]
6. Liu, B.; Yao, X.; Lin, Y.; Wu, W.; Guedes Soares, C. Experimental and numerical analysis of ultimate compressive strength of long-span stiffened panels. *Ocean Eng.* **2021**, *220*, 109633. [CrossRef]
7. Sumi, Y.; Fujikubo, M.; Fujita, H.; Kawagoe, Y.; Kidogawa, M.; Kobayashi, K.; Nakano, T.; Iwano, J.; Takahira, T.; Tamura, K. *Final Report of Committee on Large Container Ship Safety*; Committee on Large Container Ship Safety: Tokyo, Japan, 2015.
8. Fukumoto, Y.; Kusama, H. Local instability tests of plate elements under cyclic uniaxial loading. *J. Struct. Eng.* **1985**, *111*, 1051–1067. [CrossRef]
9. Cui, H.; Ding, Q. Ultimate strength and fracture failure of hull stiffened plates based on plastic accumulation under cyclic loading. *Ocean Eng.* **2022**, *261*, 112016. [CrossRef]
10. Chen, X.; Yue, J.; Song, Z.; Xu, R.; Rong, M. Study on ultimate strength for stiffened plates with elasto-plastic damages. *Ocean Eng.* **2023**, *279*, 114531. [CrossRef]
11. Li, D.; Chen, Z.; Chen, X. Numerical investigation on the ultimate strength behaviour and assessment of continuous hull plate under combined biaxial cyclic loads and lateral pressure. *Mar. Struct.* **2023**, *89*, 103408. [CrossRef]
12. Chaboche, J.L.; Van, K.D.; Cordier, G. Modelization of the strain memory effect on the cyclic hardening of 316 stainless steel. In Proceedings of the Transactions of the International Conference on Structural Mechanics in Reactor Technology, Berlin, Germany, 13–17 August 1979.
13. Li, S.; Hu, Z.; Benson, S. An analytical method to predict the buckling and collapse behaviour of plates and stiffened panels under cyclic load. *Eng. Struct.* **2019**, *199*, 109627. [CrossRef]
14. Cui, H.; Chen, Z.; Hu, R.; Ding, Q. Ultimate strength assessment of hull girders considering elastic shakedown based on Smith's method. *Ocean Eng.* **2024**, *293*, 116695.
15. Iijima, K.; Fujikubo, M. Cumulative collapse of a ship hull girder under a series of extreme wave loads. *J. Mar. Sci. Technol.* **2015**, *20*, 530–541. [CrossRef]

16. Zhang, X.; Paik, J.K.; Jones, N. A new method for assessing the shakedown limit state associated with the breakage of a ship's hull girder. *Ships Offshore Struct.* **2016**, *11*, 92–104.
17. Cui, H.; Yang, P. Ultimate strength assessment of hull girder under cyclic bending based on smith's method. *J. Ship Res.* **2018**, *62*, 77–88. [CrossRef]
18. Hu, K.; Yang, P.; Xia, T.; Song, Y.; Chen, B. Numerical investigation on the residual ultimate strength of cracked stiffened plates under extreme cyclic loads. *Ocean Eng.* **2022**, *244*, 110426. [CrossRef]
19. Liu, B.; Guedes Soares, C. Ultimate strength assessment of ship hull structures subjected to cyclic bending moments. *Ocean Eng.* **2020**, *215*, 107685. [CrossRef]
20. Li, S.; Hu, Z.; Benson, S. Progressive collapse analysis of ship hull girders subjected to extreme cyclic bending. *Mar. Struct.* **2020**, *73*, 102803. [CrossRef]
21. Deng, H.; Yuan, T.; Gan, J.; Liu, B.; Wu, W. Experimental and numerical investigations on the collapse behaviour of box type hull girder subjected to cyclic ultimate bending moment. *Thin Wall. Struct.* **2022**, *175*, 109204. [CrossRef]
22. Song, S.; Ehlers, S.; Von Bock Und Polach, F.; Braun, M. Ultra-low cycle fatigue of ship hull structure—An alternately-cyclically loaded four-point bending test of a large box girder. *Mar. Struct.* **2025**, *100*, 103732. [CrossRef]
23. Chen, Z.; Li, D.; Li, J.; Yi, J. The influence of welding-induced 3D residual stress and distortion on the ultimate strength of multi-stiffened thin plate structures under cyclic load. *Ocean Eng.* **2024**, *311*, 118797. [CrossRef]
24. Li, D.; Chen, Z. Progressive collapse response and ultimate strength evaluation of stiffened plates with welding residual stress under combined biaxial cyclic loads and lateral pressure. *Mar. Struct.* **2025**, *99*, 103703. [CrossRef]
25. Cui, H.; Hu, R.; Chen, Z.; Zheng, C. Research on ultimate strength of hull girder considering initial imperfections under monotonic/cyclic bending moments—A bulk carrier case. *Ocean Eng.* **2024**, *311*, 118862. [CrossRef]
26. Xu, M.C.; Garbatov, Y.; Guedes Soares, C. Residual ultimate strength assessment of stiffened panels with locked cracks. *Thin Wall. Struct.* **2014**, *85*, 398–410. [CrossRef]
27. Ao, L.; Wang, D.Y. Ultimate torsional strength of cracked stiffened box girders with a large deck opening. *Int. J. Nav. Archit. Ocean Eng.* **2016**, *8*, 360–374. [CrossRef]
28. Ao, L.; Wu, H.; Wang, D.Y.; Wu, W.G. Evaluation on the residual ultimate strength of stiffened plates with central dent under longitudinal thrust. *Ocean Eng.* **2020**, *202*, 107167. [CrossRef]
29. Shi, X.H.; Zhang, J.; Guedes Soares, C. Numerical assessment of experiments on the residual ultimate strength of stiffened plates with a crack. *Ocean Eng.* **2019**, *171*, 443–457. [CrossRef]
30. Feng, G.; Wang, Y.; Garbatov, Y.; Ren, H.; Guedes Soares, C. Experimental and numerical analysis of crack growth in stiffened panels. *Ships Offshore Struct.* **2021**, *16*, 980992. [CrossRef]
31. Xia, T.; Yang, P.; Song, Y.; Hu, K.; Qian, Y.; Feng, F. Ultimate strength and post ultimate strength behaviors of hull plates under extreme longitudinal cyclic load. *Ocean Eng.* **2019**, *193*, 106589. [CrossRef]
32. Hu, K.; Yang, P.; Xia, T.; Qin, D. Ultimate strength assessment of cracked stiffened box girders subjected to extreme cyclic bending moments. *Ocean Eng.* **2022**, *256*, 111496. [CrossRef]
33. Xia, T.; Yang, P.; Cui, H.; Song, Y. Experimental research on ultimate strength behaviors of cracked plates under uniaxial cyclic load. *Ocean Eng.* **2025**, *322*, 120514. [CrossRef]
34. Hu, K.; Zhang, F.; Xu, R.; Cui, H.; Yang, P. Experimental study on the ultimate strength of box-type hull girders subjected to extreme cyclic bending moments. *Ocean Eng.* **2025**, *339*, 122044. [CrossRef]
35. *GB/T 228.1*; Metallic Materials-Tensile Testing, Part I: Method of Test at Room Temperature. Standards Press of China: Beijing, China, 2021. (In Chinese)
36. Xu, S.; Liu, B.; Garbatov, Y.; Wu, W.; Guedes Soares, C. Experimental and numerical analysis of ultimate strength of inland catamaran subjected to vertical bending moment. *Ocean Eng.* **2019**, *188*, 106320. [CrossRef]
37. Liu, B.; Villavicencio, R.; Zhang, S.; Guedes Soares, C. A simple criterion to evaluate the rupture of materials in ship collision simulations. *Mar. Struct.* **2017**, *54*, 92–111. [CrossRef]
38. Paik, J.K.; Lee, D.H.; Noh, S.H.; Park, D.K.; Ringsberg, J.W. Full-scale collapse testing of a steel stiffened plate structure under cyclic axial-compressive loading. *Structures* **2020**, *26*, 996–1009. [CrossRef]
39. Song, Z.J.; Liu, Q.C.; Xu, R.J.; Yang, X.; Yue, J.X. Ultimate strength attenuation behaviours of stiffened panels under cyclic extreme loads based on test and numerical simulations. *Ocean Eng.* **2025**, *321*, 120447. [CrossRef]

Disclaimer/Publisher's Note: The statements, opinions and data contained in all publications are solely those of the individual author(s) and contributor(s) and not of MDPI and/or the editor(s). MDPI and/or the editor(s) disclaim responsibility for any injury to people or property resulting from any ideas, methods, instructions or products referred to in the content.